5-2019

TixZr(1-x)N Thin Films for Advanced Plasmonic Materials

Susan R. Schickling
The University of Tennessee, Knoxville, sschickl@vols.utk.edu

Codi Ferree
The University of Tennessee, Knoxville, cferree@vols.utk.edu

Amy Godfrey
The University of Tennessee, Knoxville, agodfre3@vols.utk.edu

Andre Hillsman
The University of Tennessee, Knoxville, ahillsma@vols.utk.edu

Hannah Robinson
The University of Tennessee, Knoxville, hrobins7@vols.utk.edu

$Ti_xZr_{(1-x)}N$ Thin Films for Advanced Plasmonic Materials

Codi Ferree[1], Amy Godfrey[1], Andre Hillsman[1], Hannah Robinson[1], Susan Schickling[1], David Garfinkle[1], Philip Rack[1], Jason Fowlkes[1]

[1]Department of Materials Science and Engineering, The University of Tennessee, Knoxville, TN

ABSTRACT

Traditionally, gold and silver have been used as plasmonic materials due to their high electrical conductivities and low dielectric losses. Refractory ceramics, such as titanium nitride (TiN) and zirconium nitride (ZrN), combine these electrical properties with an increased melting temperature, allowing them to be used in higher temperature applications. Additionally, the $Ti_xZr_{(1-x)}N$ ternary system may allow for the tunability of the optical properties. Combinatorial thin film sputtering was utilized to produce a $Ti_xZr_{(1-x)}N$ thin film gradient to explore refractory plasmonic materials. Thermodynamically, the $Ti_xZr_{(1-x)}N$ system forms a solid solution outside of a miscibility gap. Thus, the sample was annealed at a high temperature to enhance crystallization and attempt to form separate phases within the miscibility gap. The as-deposited film will be characterized using scanning electron microscopy (SEM), energy dispersive x-ray spectroscopy (EDS), x-ray diffraction (XRD), and spectroscopic ellipsometry.

I. Background and Introduction

A. *Plasmonics*

Plasmonics is a field dedicated to the study of the plasmon and its uses. Plasmonic devices are designed to make use of the relationship between the electromagnetic field and a material's free electrons. When the proper conditions are present and the variables are well controlled, plasmons can be created [1].

A plasmon is a polar quasiparticle produced by striking the surface of a material with light [2]. The electromagnetic field from the light stimulates the free electrons on the surface of the material to begin to oscillate, as seen in Figure 1. The frequency at which the electrons oscillate determines whether a plasmon will form or not. If the frequency is within the material's natural plasma range, then a plasmon will be produced. This process is generally easier in bulk materials, where the electrons have the space needed to move about freely. However, in nanomaterials, plasmon production is more difficult, as the free electrons in the material are restricted to a smaller area than they are in a bulk material [1].

A plasmon will only absorb the light that oscillates at the same frequency as the plasmon itself. Any other light incident on the surface will be reflected/absorbed. This can be useful for producing electronics that function at the nanoscale (below the diffraction limit) or that have increased efficiency. Additionally, plasmon resonance can be used to detect the presence of chemical and biological toxins in a material, as toxins will alter the reflection angle of the non-absorbed incident light. A change in the reflection angle will indicate the presence of a toxin [1].

Currently, gold and silver are the most common plasmonic materials in use. This is due to the metals' high electrical conductivity, which is coupled with a low dielectric loss. Unfortunately, gold and silver both have relatively low melting temperatures, thereby limiting their use in higher temperature applications. Transition metal nitrides, on the other hand, are generally used as refractory materials and are therefore appropriate for use at higher temperatures. Materials such as TiN, ZrN, and HfN in particular combine the electrical properties of gold and silver with improved thermal properties and higher corrosion resistance. Utilizing these ceramics could allow for the production of plasmonic devices suitable for high temperature or heavily corrosive environments [3].

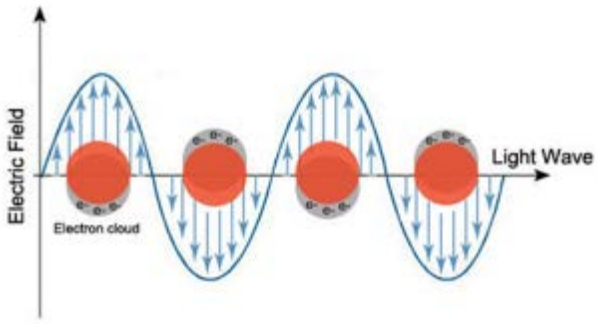

Figure 1: Free electrons oscillate in response to the electromagnetic field. If this oscillation is in the correct frequency, a plasmon will be produced [4].

B. *Sputtering*

Sputtering is a physical vapor deposition technique commonly used for growing thin films. The technique relies on the ion bombardment of ionizing gas particles onto a target that subsequently emits particles of the depositing element onto a substrate. In order for the process to occur, there must be a momentum exchange between the ions and atoms in the target material. The kinetic energy of the incoming ions must exceed the binding energy of the target atoms/compound. Atoms from the target (cathode) are ejected and condensed from the gas

phase onto a substrate (anode) after transport through the plasma or glow discharge [5]. To generate the plasma, the chamber is filled to an appropriate pressure with an inert gas such as argon which is ionized when a voltage is applied across the cathode and anode prior to deposition. Free electrons are responsible for the ionization and as a result, the positively charged ion atoms are accelerated towards the negatively charged target. A series of collisions between the ions and the target surface allow atoms to be sputtered from the target. Common applications for sputtering include depositing thin films for semiconductor and superconducting devices, transistors, other microelectronic devices, optical coatings, and magnetic media applications.

Sputtering is done using either DC voltage (DC sputtering) or AC voltage (RF sputtering) where the alternating current enables insulating materials to be deposited. Figure 2 illustrates the sputtering process, where argon (Ar) is used as the primary sputtering gas. The Ar gas particles are ionized by the applied voltage, accelerated toward the target, and cause atoms from the target material to be ejected from the target, transported through the plasma and eventually condensed at the substrate. These particles from the target material collect and create a thin film while some of the ionized gas particles interact at the chamber walls or are pumped from the chamber.

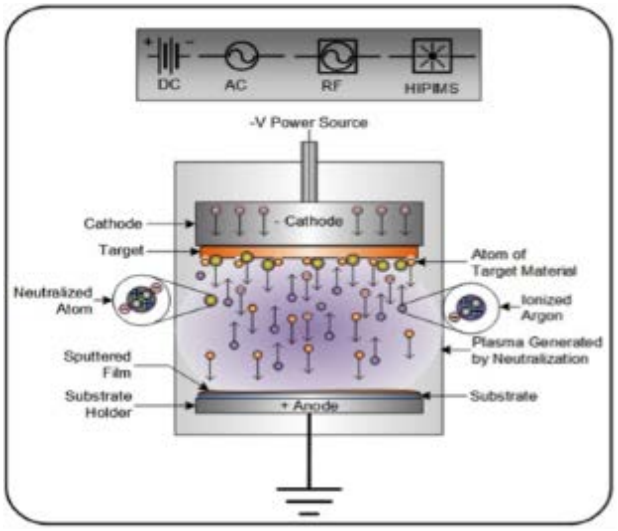

Figure 2: Image of the sputtering process inside the sputtering chamber walls including the inert gas, target, and substrate. [6]

There is a specific case of sputtering known as reactive sputtering. In this process a reactive gas is also incorporated into the chamber and activated by the plasma and chemically reacts with the target material in the same manner as normal sputtering. For example, a silicon target reactively sputtered with oxygen gas can produce a silicon oxide film, or with nitrogen gas can produce a silicon nitride film. Figure 3 illustrates the reactive sputtering process where oxygen is used as the reactive gas and chemically reacts with the target material. The oxygen particles bind with the target atoms and sputter onto the substrate in order to grow an oxide.

With reactive sputtering the reactive gas is introduced into the plasma and mixed with an inert gas such as argon, xenon, and krypton [7]. These noble gases are preferred due to their low reactivity with other elements. Composition control of the overall film can be achieved by controlling the relative amounts of inert and reactive gases (ie N_2 vs Ar flow). While some processes may involve only using a reactive gas, with the addition of an inert gas, the partial pressure of the reactive gas is one of the variables that will influence the stoichiometry and characteristics of the film [6]. This is a popular technique for growing oxides (O_2), nitrides (N_2), carbides (CH_4), and other compounds for a variety of applications.

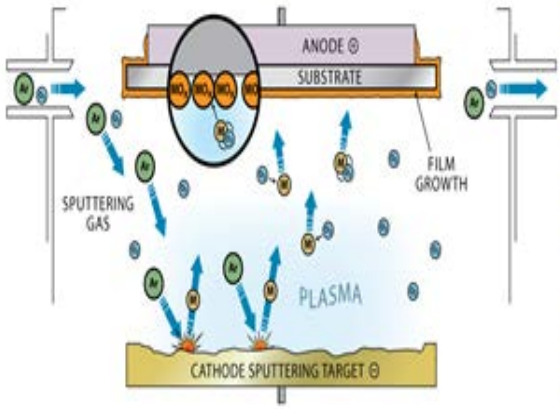

Figure 3: Image of the sputtering process inside the sputtering chamber walls including the inert and reactive gases, target, and substrate. [7]

Substrate selection is an important component. Each element has a degree of reactivity relative to one another. This influences the ability of each element's prominence onto the substrate. The degree of prominence is referred to as the "sticking parameter". Silicon is a popular choice of interest due to the low reactivity of silicon, but in some instances silicon dioxide, an oxide layer, or another element may be grown or deposited in order to improve the adhesion between the depositing element and the substrate.

A technique known as combinatorial sputtering is sometimes implemented. When co-sputtering inside the chamber with sputtering guns on opposing ends, the target atoms approach the substrate in a manner that makes each ends of the substrate rich with the target element closest to the substrate. This allows a composition gradient across the substrate surface and the sample to mimic that of a phase diagram.

The substrate temperature itself can also influence film quality in terms of uniformity and surface roughness. Higher temperatures have been found to decrease surface roughness which is typically desired although phase transformations in the case of co-sputtering must be taken into account.

Figure 4: Image of the AJA International ATC 2000 Sputtering System.

Sputtering must be operated at low pressures requiring a sufficient vacuum system. Pressure requirements are usually at least 10^{-3} Torr - 10^{-7} Torr. This is done to ensure a clean environment in the sputtering chamber and protect the sample from any impurities that could possibly contaminate the sample. Figure 3 is an image of a sputtering system used for thin-film experiments. To the far left is the sputtering chamber. Located in the middle is the load-lock chamber. This load-lock is commonly used, but not always, as a medium to allow loading and unloading of the sample while maintaining the sputtering chamber at a low, experimental pressure. There is a stainless steel valve between the load-lock and sputtering chambers to allow the distinct pressure differences between chambers.

C. Energy Dispersive X-Ray Spectroscopy

Energy Dispersive x-ray Spectroscopy (EDS) is a characterization technique that analyzes the chemical composition of a sample. After preparation, the thin film is loaded into a scanning electron microscope (SEM). The scanning electron beam generates the high energy electrons required to produce the characteristic x-rays. The energetic electrons (typically 10-30 keV) are bombarded onto the sample using a high energy focused electron beam that causes electrons in an elemental shell to move to higher energy levels which relax back down to the ground state and; ultimately produces characteristic and continuous x-rays. X-rays with an appropriate solid angle is absorbed by the detector and the energy from that x-ray is then transformed into an electrical voltage. The electrical voltage correlates with the particular characteristic x-ray, which is representative of a certain element. Multiple peaks are produced to form an EDS spectrum that is then analyzed by the computer software. The plot has energy in keV on the x-axis and the x-ray count on the y-axis. Since every element has electron energy levels with characteristic binding energies, the computer can determine the element(s) present in the area scanned of that sample. The computer software is also able to report atomic percentages for each element present based on calculated sensitivity factors [8].

An EDS instrument has three main components including a detector, pulse processor, and a multiple channel analyzer. The x-ray detector converts the x-rays emitted into the electronic signals. A pulse processor then measures the electronic signals and determines the energy for a particular x-ray. Finally, the data computed is interpreted and displayed for the user to read by the multiple channel analyzer [9]. A schematic of this process is displayed in Figure 5.

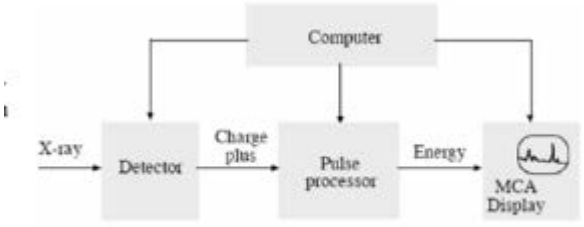

Figure 5: A schematic of the process starting from the detection and interpretation of a characteristic x-ray using an EDS instrument [9].

Thin films that have undergone reactive sputtering can be analyzed via EDS for fast chemical analysis. The reactive sputtering deposition is used to produce films with controlled composition or stoichiometry. The layer composition for our system generates a combinatorial gradient across the sample ($Ti_xZr_{1-x}N$). One side of the sample should be ZrN-rich and the other TiN-rich with a gradient between the two ends. When multiple samples are produced using reactive sputtering and stoichiometry is important, EDS is a fast way to examine the varying composition. Although analysis of a sample using EDS is a quick tool to identify elements and composition, results can have inaccuracies. The largest limitation is the overlying peaks for different elements. If an element has a low atomic number (typically below Z=6), the corresponding energy peak produced may not be present in the EDS spectrum. Another limitation is the thickness must be thick enough for the electron to generate a sufficient number of electrons and not get a convoluting spectrum from the underlying substrate.

D. X-Ray Diffraction of Thin Film Materials

XRD (X-ray powder diffraction) is a method in which the crystal structure or atomic arrangement of a certain material causes an incident X-ray beam to diffract; the diffraction angles and intensities are measured and used to create XRD patterns [10]. Because measured diffraction peak positions and intensities are unique for each crystalline phase, the foremost purpose of XRD is to identity the phases present in a sample. By detecting the atomic site positions of reciprocal lattice points in a sample, XRD can also be used to classify its crystal system and lattice constants [11].

Although XRD is traditionally performed using powder samples, it can be used to analyze a plethora of materials

including thin films. XRD is a useful tool for the characterization of thin film materials because it is a non-destructive technique that allows data collection under typically atmospheric pressure. The incident angle of the X-ray beam can be adjusted in order to control the depth at which the sample will be analyzed [12].

The analysis of thin films through XRD can be more challenging than conventional powder samples. Symmetrical reflection measurement geometry, where the incident and diffracted angles are equivalent, is traditionally used to investigate lattice planes parallel to the surface of a powder sample. When thin films exhibit a strong preferred orientation, a symmetrical reflection measurement can only be used to detect one set of lattice planes. An asymmetrical reflection measurement can be used instead, where the incident angle is stationary and shallow. This method is referred to as grazing incidence X-ray diffraction (GIXRD). Symmetrical and asymmetrical measurements are known as out-of-plane measurements because the normal direction of the lattice planes comes out of the surface of the sample. Recent technological advancements have made it possible to also examine the lattice plane perpendicular to the surface of the sample. This type of measurement is called in-plane measurement because the normal direction of the lattice planes is parallel to the surface of the sample [12]. Schematic diagrams of out-of-plane and in-plane geometries can be found in Figure 6.

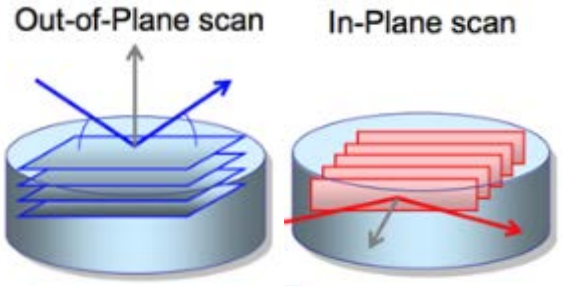

Figure 6: Two different XRD scanning modes used to investigate thin films: out-of-plane and in-plane measurements. In an out-of-plane scan the observed lattice plane is parallel to the surface of the sample, while the observed plane in an in-plane scan is perpendicular to the surface [11].

E. Spectroscopic Ellipsometry

Spectroscopic ellipsometry is a non-destructive, noncontact, and non-invasive optical characterization technique used on thin film samples. Spectroscopic ellipsometry can be utilized to characterize composition, roughness, thickness, crystallinity, dopant concentration, electrical conductivity, etc. For the purpose of the experiment measuring the change in polarization as light is reflected from the sample to determine its optical properties is of the greatest interest. The goal of this characterization technique is to determine the samples optical properties by determining its refractive index, n, and the extinction coefficient, k. Thus, the complex refractive index, N, can be determined using the following equation: N = n – ik. To measure this change in polarization state the sample is exposed to electromagnetic radiation that has been linearly polarized by a polarizer. This polarized beam strikes the sample at an incidence angle. Once the beam contacts the sample, the polarization changes and the beam is reflected at a reflection angle. This reflected beam passes through another polarizer; a phase modulator, only some ellipsometers use a modulator; through an analyzer, and finally on to a detector, as seen in Figure 7.

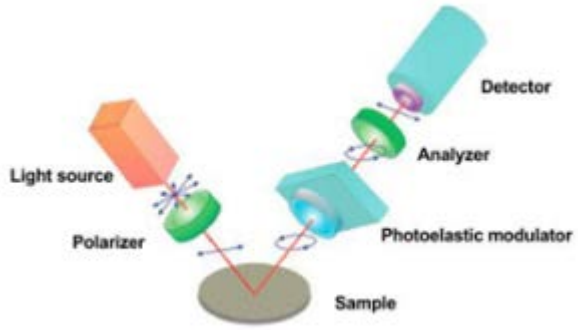

Figure 7: Schematic set-up of ellipsometry [14].

The ellipsometric angles, Δ and Ψ, are now measured and used to solve for n and k. The Δ angle is defined as $\Delta = \delta_{in} - \delta_{out}$, where δ_{in} is the difference of the phases of the parallel and perpendicular components of the incoming waves and δ_{out} is the corresponding outgoing wave phase difference. The Ψ and is defined as $\tan\psi = {|R_p|}/{|R_s|}$, where Rp and Rs are the reflection coefficients of the parallel and polarized beam.

The resultant data is then compared to a known model for comparison and identification. This technique can be performed in-situ or ex-situ as well as in static or kinematic mode.

F. Applications of Plasmonic Materials

There are a number of applications of plasmonic materials, ranging from medical applications to data storage. For example, plasmonics can be used to detect chemical and biological toxins in materials. This detection relies on the phenomenon of plasmon resonance. If a toxin is present in a material, it will alter the oscillation frequency of the plasmons, thereby changing the light reflection angle of the plasmons from their characteristic angles. Plasmonics can also be utilized in communications. High strength limitation of the effects of the electromagnetic field to an area below the diffraction limit, coupled with high oscillation speeds, allows for plasmonic materials to be utilized in optical signal processing.

Additionally, plasmonic materials can be used in data storage applications. Such applications involve localized heating of the material, thereby requiring the material to be able to withstand high temperatures. However, the two most commonly used plasmonic materials, gold and silver, have relatively low melting temperatures, rendering them less than ideal for such applications. Refractory materials, such as TiN and ZrN may

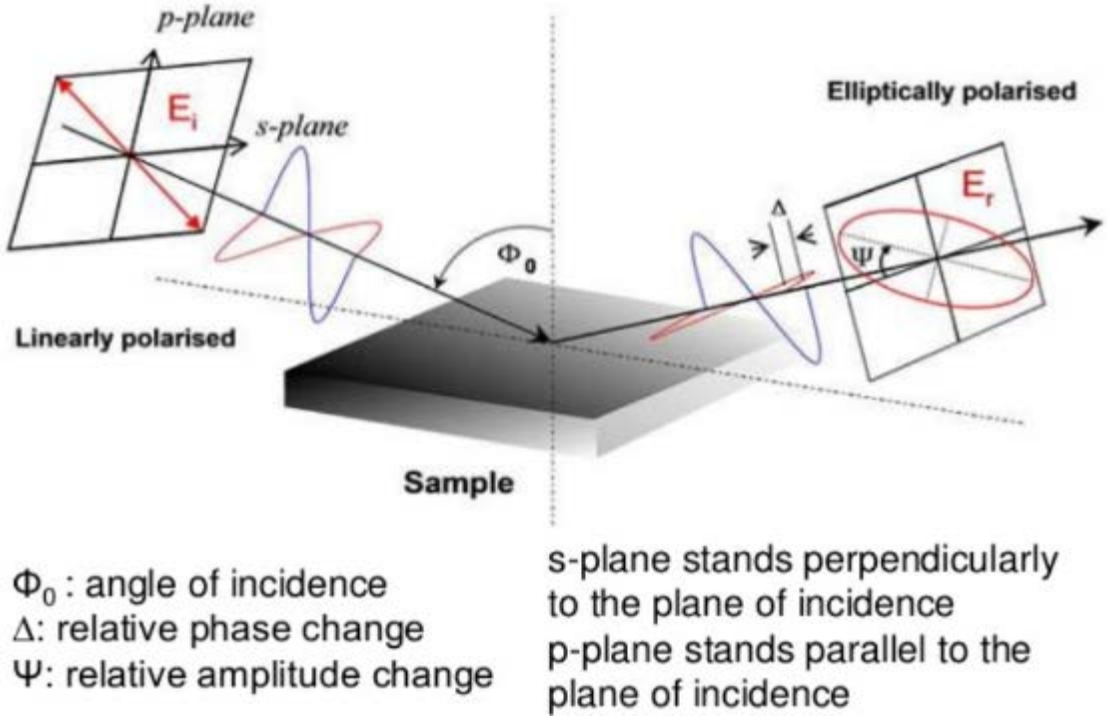

Figure 8: Principle of ellipsometry [16].

provide the necessary thermal stability required for these applications.

G. Why These Nitrides?

As with any material, the properties of TiN and ZrN are determined by their structures. Both nitrides have rocksalt crystal structures, which lends itself well to forming ternary or pseudo-binary conductive films. Additionally, titanium and zirconium fall in the same column on the periodic table, allowing them to have the same electron configuration of d^2s^2. These partially filled *d* electron orbitals give the two metals high electrical conductivities. TiN and ZrN also have good mechanical, thermal, and chemical properties, which, when combined with their crystal structure, makes them stable materials and allows them to be used in a number of applications [1].

The plasmonic qualities of a material are determined by its conduction electron density, which is in turn dictated by which material is chosen. Different transition metals therefore have different conduction electron densities. When ternary conductive films are produced, the plasmon resonance can be controlled by using different metals. Titanium and zirconium are both group IVb transition metals and a ternary conductive alloy of this combination would have a set conduction electron density that produces optical and plasmonic effects within the visible range. Replacing one of the two metals with a group Vb metal, such as vanadium, would shift the plasmon resonance toward a blue wave frequency, while replacing one of the metals with a group III element, such as aluminum, would shift it toward the infrared [1].

The combination of TiN and ZrN is useful for plasmonic applications mainly due to the individual properties of the nitrides. TiN is a tunable material, which can be combined with nitrides of other element groups to form plasmonic films in a variety of frequency ranges. ZrN, meanwhile, is a very stable nitride and can form a solid solution with TiN at higher temperatures, as seen in Figure 9. These material properties grant a ternary film consisting of TiN and ZrN the ability to be used in refractory plasmonic applications, as it would be able to withstand high temperatures and would maintain its stability and tunability when other films may not [1].

II. Problem Statement

Two of the most common plasmonic materials currently in use are gold and silver. These two transition metals have high electrical conductivities coupled with low dielectric loss, which make them excellent for creating plasmons. However, gold and silver have relatively low melting temperatures, which limit their use in extreme conditions. Transition metal nitrides (TMNs), such as TiN or ZrN, are refractory materials that have a balance of desired properties. These materials blend the good electrical qualities of gold and silver with the ability to withstand high temperature and highly corrosive environments. In order for TiN and ZrN to be considered plasmonic materials, however, they must have certain optical properties. TiN and ZrN thin films will be sputtered in a gradient from TiN to ZrN across the width of a silicon wafer that has been oxidized to produce a thin coating of silicon dioxide. The as-deposited coating will be characterized using scanning electron microscopy (SEM), energy dispersive x-ray spectroscopy (EDS), x-ray diffraction (XRD), and spectroscopic ellipsometry (SE). The film will be annealed to determine if the film can achieve crystallinity without non-ambient temperature

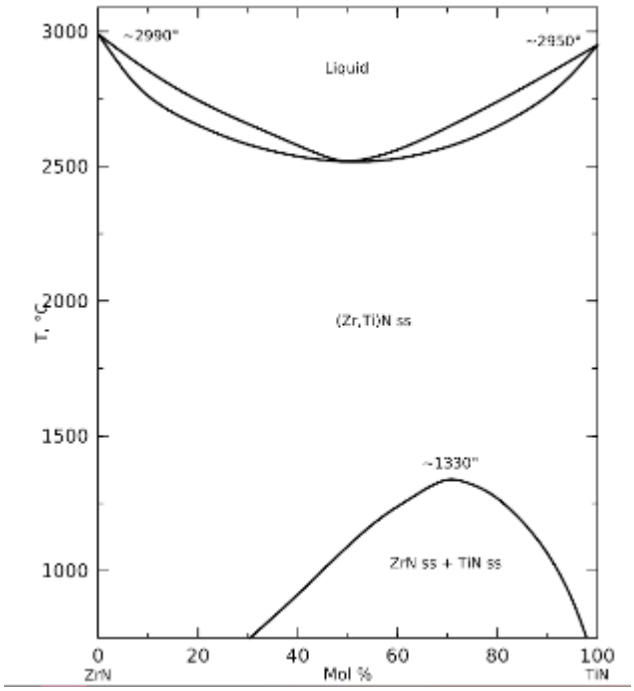

Figure 9: Phase diagram of the TiN-ZrN ternary system. At lower temperatures, there is a miscibility gap where the two nitrides do not form a solid solution. However, at higher temperatures, ZrN is soluble in TiN, forming a solid solution that may be useful for refractory plasmonic applications [16].

sputtering. The annealed film will be characterized in the same manner as the as-deposited film.

III. Non-Scientific Implications

Using new materials to produce plasmonics may reduce the cost of such products, especially since the current materials in use, gold and silver, are precious metals. This designation increases the cost of use, and a switch to lower cost materials may make plasmonic devices more affordable. Changing the material may also affect international trade, as countries that produce gold and silver may suddenly have to export smaller quantities. However, these considerations may not be necessary for this project, as it is more exploratory.

IV. Methods

A. Sputtering

All samples were co-sputtered with a 200 W bias on the Ti and Zr targets using AC Voltage (RF Power) with an experimental chamber pressure of 5 mTorr, and flow rates of 20 sccm Ar for the inert gas and 5 sccm N for the reactive gas. The initial chamber pressure prior to Ar and N flow was 3 x 10^{-7} Torr and the substrate temperature during sputtering was room temperature (25 °C). The first sample was sputtered for an hour. Based on the deposition rates, the anticipated film thickness should be near 150 nm. Since combinatorial sputtering is used, there should be a composition gradient of TiN and ZrN across the substrate that will resemble a phase diagram. To better suit the grazing technique for XRD, the film thickness needed to be higher, therefore the second and third samples were sputtered for three hours where the anticipated film thickness is 300 nm.

B. Scanning Electron Microscopy and Energy Dispersive X-Ray Spectroscopy

After the sputtering process was accomplished, scanning electron microscopy (SEM) and energy dispersive electron microscopy (EDS) was used to obtain morphological and chemical data. The sample was cut in half and nine scratches were made along the straight edge of each half, roughly 1 cm apart. The ZEISS MERLIN, located at Oak Ridge National Laboratory, was used to analyze both the titanium and zirconium rich sides of the wafer. An even thickness layer was expected throughout the wafer, and distinct morphological changes were expected across the material gradient. The voltage used was 10 keV, the magnification was 100 kX, and the scale was 100 nm.

The ZEISS EVO (Sample 1) instrument, located at the Joint Institute of Advanced Materials (JIAM), and the ZEISS MERLIN (Samples 2 and 3), located at Oak Ridge National Laboratory, were required for EDS measurements. EDS was run near each scratch to obtain the elemental composition of the wafer at each point. A voltage of 10 keV and a magnification of 100 kX was used for the EDS measurements. The chosen voltage is roughly double that of the characteristic peak of titanium and was chosen to minimize the contribution from the substrate in the resultant spectra. Peaks were expected at 4.97 keV for titanium, 2.535. keV for zirconium, and 0.397 keV for nitrogen. Since the wafer is made of silicon with a silicon dioxide layer, the presence of silicon peaks around 1.840 keV and oxygen peaks around 0.533 keV was anticipated in the resultant EDS spectra. Sample thickness is important, as the peaks from the substrate must be limited and the nitrogen Kα and titanium Lα peaks must be distinct.

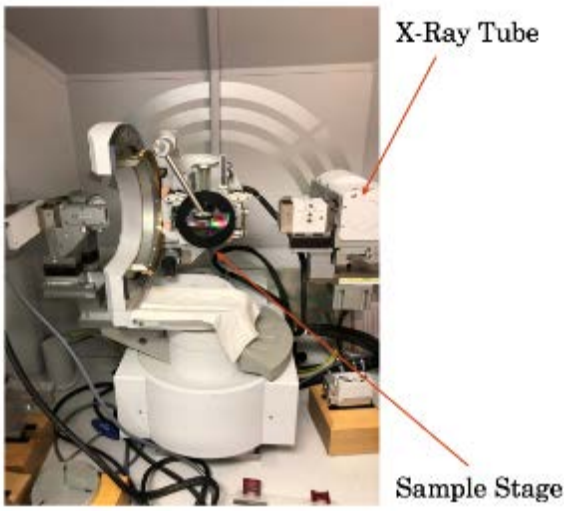

Figure 10: The X'Pert³ MRD will be used to analyze the structure of the sample.

C. X-Ray Diffraction

The X'Pert³ MRD system, located at JIAM was used to perform structural analysis and confirm the presence of a combinatorial gradient across the sample through the utilization of GIXRD. The instrument parameters are listed in Table I. XRD measurements were taken in between each scratch along the sample. A labeled schematic of the diffractometer we will be using can be found in Figure 10. The resulting XRD peaks were analyzed using Panalytical HighScore Plus software.

Table I: XRD Instrument Parameters

Voltage (kV)	45
Current (mA)	40
Step Size (°)	0.06
Scan Range (°)	24 – 70
Anode Material	Cu
Kα – 1 (Å)	1.540598
Omega (°)	2.55

D. Spectroscopic Ellipsometry

Ellipsometry was performed using a J. A. Woollam M-2000U spectroscopic ellipsometer at the Center for Nanophase Materials Science (CNMS) at Oak Ridge National Laboratory (ORNL), seen in Figure 11. A total of nine measurements were taken for each sample at intervals across the gradient from TiN rich to ZrN rich. Figure 12 shows a closer look at the sample set up for ellipsometry measurements.

E. Anneal

Sample 1 was annealed in the sputtering chamber at 700 °C for 1 hour 30 minutes at vacuum. The sample was characterized using the same methods as the as-deposited sample. Sample 1 was then annealed again at 1100 °C in Ar for one hour and characterized.

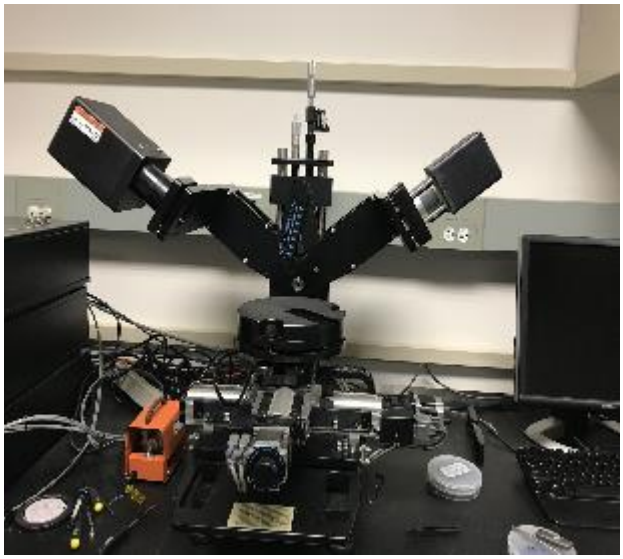

Figure 11: The J. A. Woollam M-2000U spectroscopic ellipsometer at the CNMS.

F. Additional Samples

Additional samples (Samples 2 and 3) were sputtered in order to produce a thicker film. The as-deposited films were characterized using the same methods as Sample 1. Sample 3 was also annealed at 850 °C for 3.5 hours and was subsequently characterized using SEM, EDS, XRD, and spectroscopic ellipsometry.

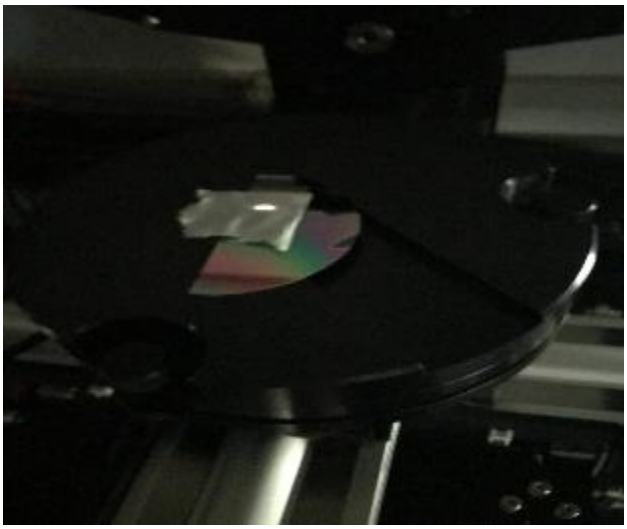

Figure 12: Sample 1 as deposited being analyzed with the ellipsometer. In this image the paper helps align the beam with the correct portion of the sample between the desired scratches.

V. Results and Discussion

A. Sample 1

Sputtering of the first $Ti_xZr_{1-x}N$ sample produced a wafer that contained a compositional gradient that contained a Zr rich side and a Ti rich side. The results of electron dispersive x-ray spectroscopy for the first sample are shown in Figure 13. The EDS results suggest that the desired combinatorial gradient along the wafer was achieved. It is clear that the Zr rich side is found near position 1 and the Ti rich side is found near position 9. The N peak is very small and is not around the energy amount for a typical N atom. It is very difficult to obtain results for N peaks due to the small atomic number. The EDS instrument used was not as precise as one would like. It was determined that to obtain a more accurate result of EDS data, the analysis would have to be done on a more accurate instrument.

Conclusion of the results displayed in Fig. 13 are confirmed by observing Table II. Figure 14 shows that at position 1 the Zr fraction is around 90% but as we increase to position 9, the Ti fraction has increased to around 90%. The nitrogen to Zr and Ti fractions is displayed in Figure 15. The graph shows that there was a consistent amount of nitrogen flowing throughout the sputtering process. The final graph, Figure 16, combines the

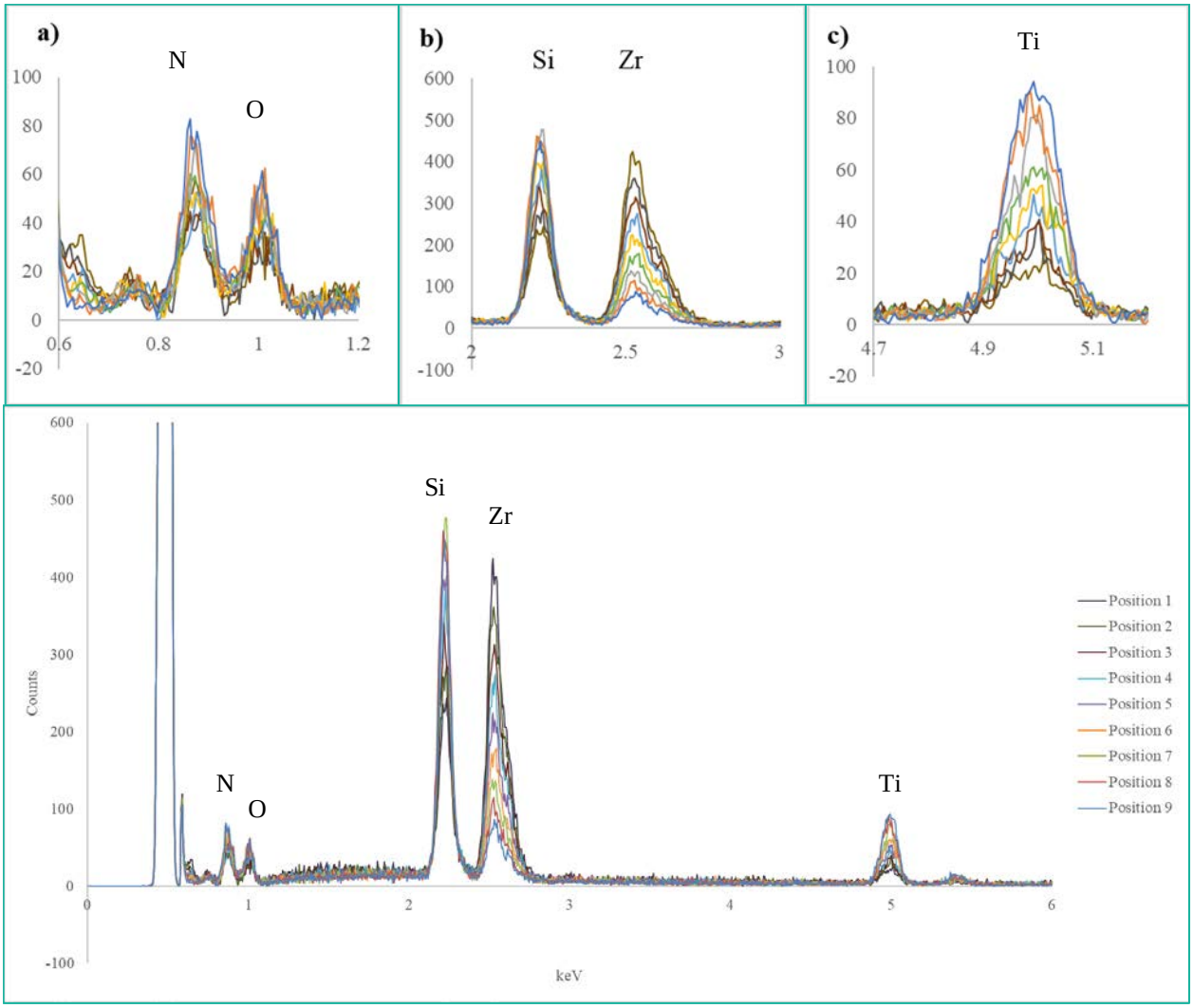

Figure 13: The EDS results for the first sputtered $Ti_xZr_{1-x}N$ sample using a ZEISS MERLIN. The nitrogen and oxygen peaks are shifted to the right when compared to literature results. The three insets a) nitrogen (N) and oxygen (O) peaks b) the Zirconium (Zr) and Silicon (Si) and c) the titanium (Ti) are required for a clearer picture of the different peaks for each position. The insets show that as the positions increase from 1 to 9 the amount of Zr reduces while the amount of Ti increase.

two data sets given in Figs. 14 and 15. The expected gradient along the wafer and the nitrogen amount required to obtain a solution of $TI_xZr_{1-x}N$ was achieved through the sputtering process.

The SEM data displayed in Figure 17 for the first sample suggests that the thickness for both Zr and Ti rich sides of the sample are not thick enough for further analyzation techniques, mainly spectroscopic ellipsometry.

Figure 18 shows the XRD patterns for each composition along the first as-deposited sample, and Figure 19 shows the XRD patterns for each composition along the first annealed sample. The XRD results for both samples suggest that a solid solution is present. The peak on the far right of Fig. 18 corresponds to Si; a large Si peak is present due to the substrate. Annealing at 700 °C had a minimal effect on the XRD data.

The (111) and (200) peaks shift left as the amount of Zr increases, as can be seen in Figures 18 and 19. When Zr is substituted for Ti in the TiN structure, strain is created within the lattice. This is because Zr atoms are larger than Ti atoms. Adding Zr to TiN increases the lattice parameter of the structure, hence the shift toward smaller 2θ positions.

The peak shift is consistent with the composition shift; however, the experimental peak positions are located outside the range of accepted literature values. This has resulted in the inability to complete Vegard's law calculations for Sample 1.

Figure 20 shows the XRD patterns for each composition along the first sample after its second anneal. The XRD results indicate that annealing at 1100 °C did not yield a solid solution. After the second anneal, the TiN and ZrN peaks begin to decompose and are less prominent than the as-deposited and

Table II: Summary of the Atomic Percent of positions 1-9 for each element. The data obtained was taken on the ZEISS MERLIN SEM instrument.

	Atomic %								
Element	**Position 1**	**Position 2**	**Position 3**	**Position 4**	**Position 5**	**Position 6**	**Position 7**	**Position 8**	**Position 9**
Silicon	21.1	30.87	25.58	33.61	33.62	35.42	33.98	34.31	25.32
Zirconium	29.28	23.66	29.26	19.26	14.05	10.79	7.32	5.74	3.25
Titanium	4.29	9.84	16.36	11.86	14.66	16.36	21.68	22.23	31.1
Nitrogen	34.47	26.22	29.26	23.4	23.61	28.35	21.93	22.9	23.46
Oxygen	10.86	9.42	8.09	11.87	14.06	14.08	15.1	14.82	16.89

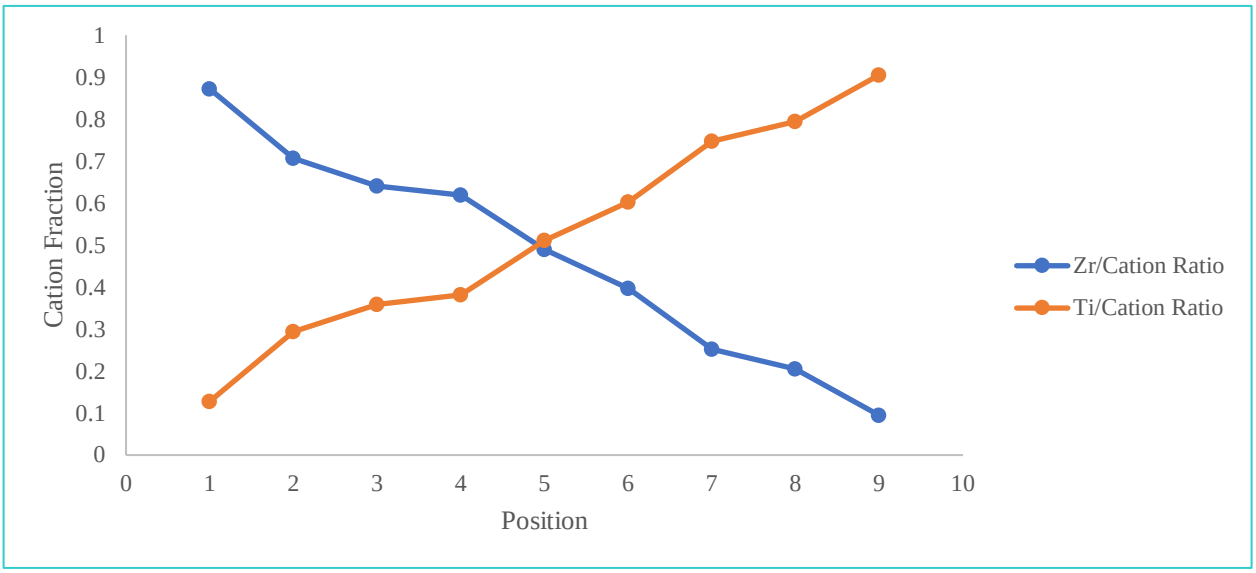

Figure 14: The cation fractions for Ti and Zr obtained for each position according to Table II. The combinatorial gradient is seen as the positions increase from 1 to 9, moving from the Zr rich side to the Ti rich side.

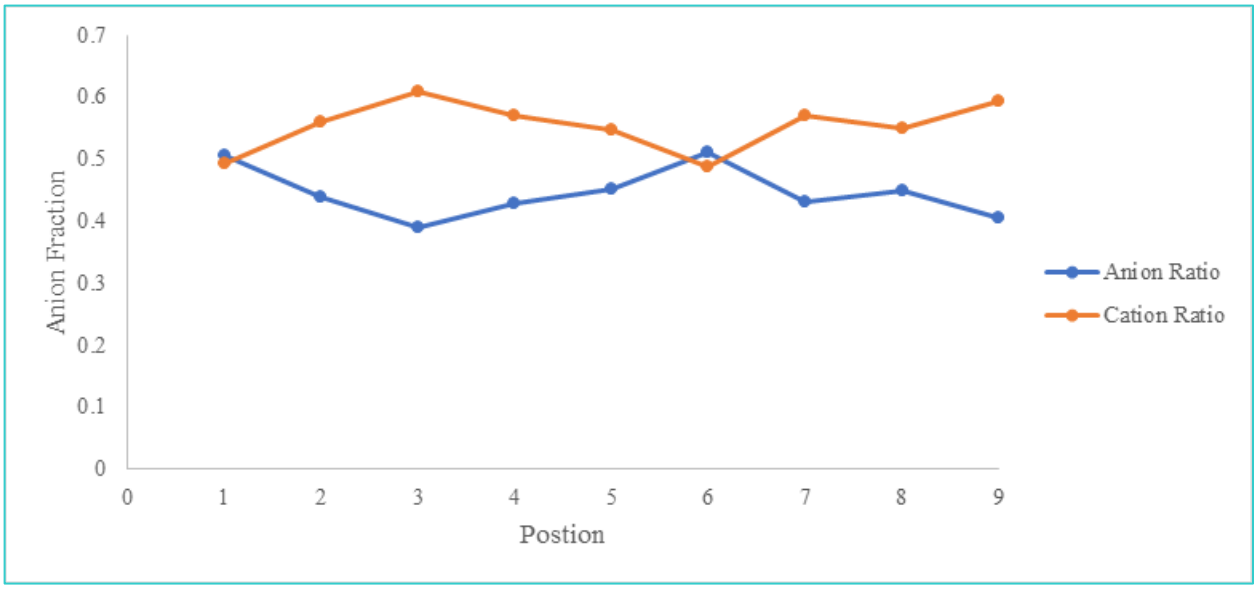

Figure 15: The cation fractions for Ti and Zr obtained for each position according to Table II. The amount of nitrogen is consistent with the amount of cation fractions.

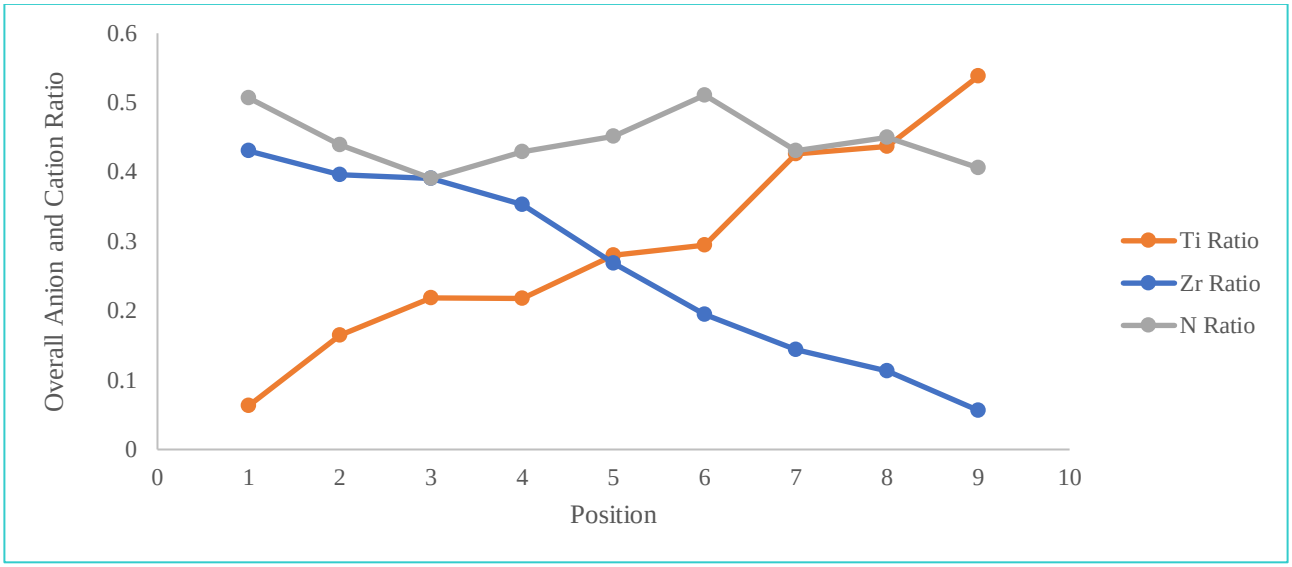

Figure 16: The overall view of the cation fractions for Ti and Zr, as well as the nitrogen fraction obtained for each position according to Table II. The amount of nitrogen is consistent, and the combinatorial gradient is achieved.

700 °C annealed samples. This could have been attributed to oxidation of Ti and Zr as the oxidation temperatures of both elements are near 900 °C. The relative amounts of TiO and ZrO in the middle positions may have caused the peaks to dissociate from the $Ti_xZr_{(1-x)}N$ lattice parameter. This unsatisfactory outcome prompted an anneal temperature less than 1100 °C for future samples.

Spectroscopic ellipsometry was performed on Sample 1 as-deposited. Measurements were taken at an angle of 70°. Sample 1 was discovered to be too thin to achieve accurate results, as there was significant interference from the substrate. The sample is also optically too thin. The e1 values are all positive, as seen in Figures 21 and 22, meaning the sample does not behave metallically. No ellipsometry was performed on the annealed sample, as the as-deposited film was already too thin. The lack of metallic behavior in the sample is due to excess oxygen in the film.

B. Sample 2

The EDS results for Sample 2 were run using the ZEISS MERLIN instrument located at Oak Ridge National Laboratory. Results for the second sample indicate that the sputtering process produced a thicker wafer, but with an inaccurate composition. The more accurate instrument produced peaks that were closer to their literature value as seen in Figure 23. The Si peak is not present which would indicate that there was no silicon dioxide contamination in the EDS

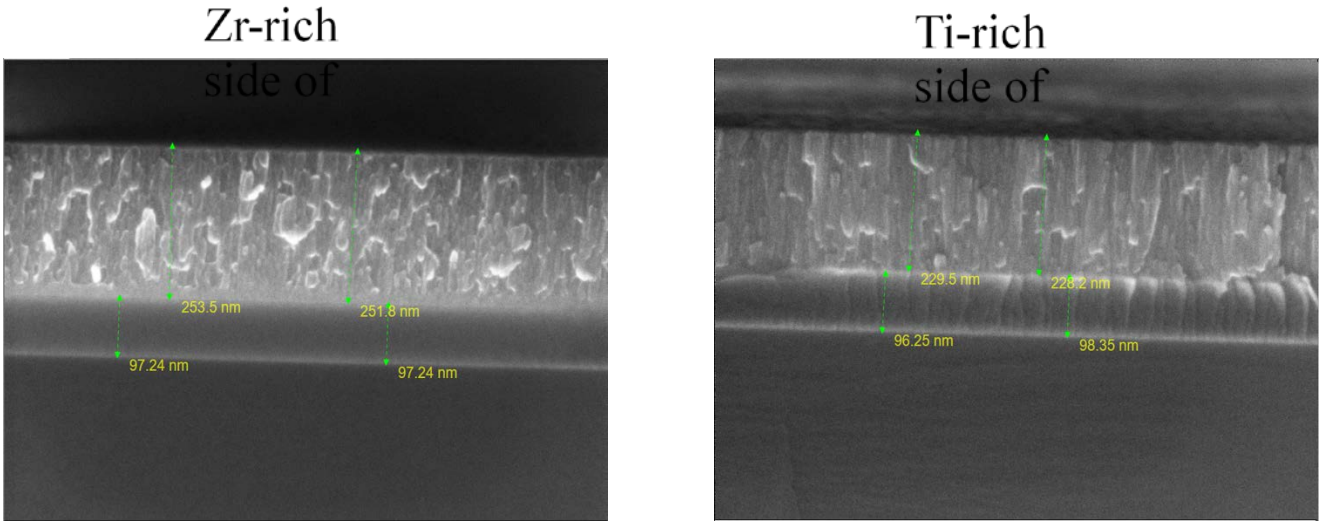

Figure 17: The ZEISS EVO SEM image using 10.0 keV at a magnification of 100.0 kX for the Zr and Ti rich sides of the first sputtered wafer. The Zr rich side is thicker than the Ti rich side, one around 250 nm and the other around 230 nm, respectively.

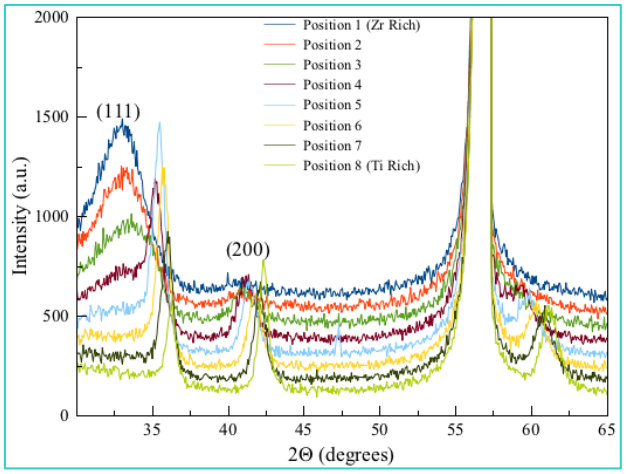

Figure 18: The diffraction pattern for the first as-deposited sample. The first prominent peak at every composition corresponds to the (111) plane, while the second, less pronounced peak corresponds to the (200) plane. The largest peak corresponds to Si.

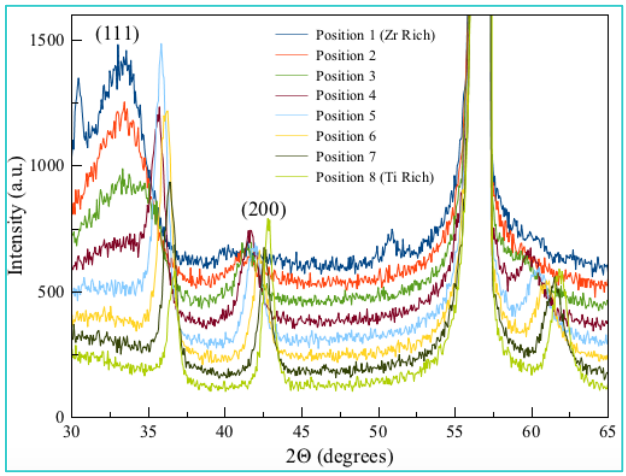

Figure 19: The diffraction pattern for the first sample annealed at 700 °C. The first prominent peak at every composition corresponds to the (111) plane, while the second, less pronounced peak corresponds to the (200) plane. The largest peak corresponds to Si.

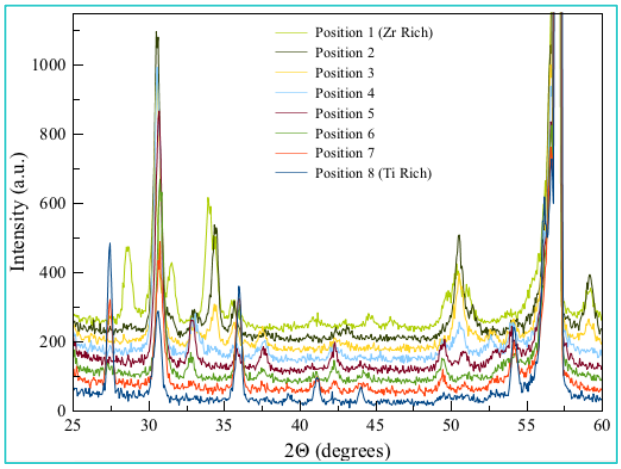

Figure 20: The diffraction pattern after the first sample underwent a second anneal at 1100 °C. The largest peak corresponds to Si.

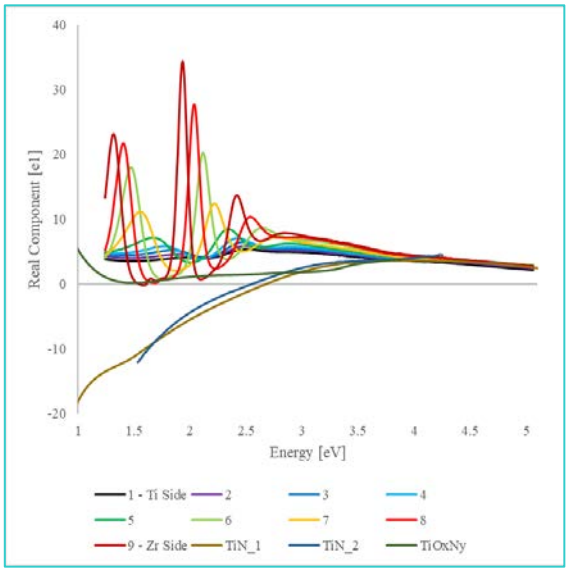

Figure 21: The real component data of ellipsometry scans performed on as-deposited Sample 1.

results. When one views Table III, however, there are large amounts of oxygen, which suggests that there was oxygen contamination sputtering. This required that a whole new wafer be sputtered to obtain the desired combinatorial gradient.

Spectroscopic ellipsometry was performed on Sample 2 as-deposited. Measurements were taken at an angle of 80°. The measurements at positions 1 and 2 indicate that the film is optically too thin at those positions. There are also visible interference patterns as a result of oxygen in the sample. The oxygen present in the SiO_2 substrate layer only accounts for some of the oxygen interference. The excess oxygen interference leads to the conclusion that there was oxygen present in the sputtering chamber during production of the sample. Additionally, the e1 values, as seen in Figures 24 and 25, are still positive, indicating that the sample does not behave metallically. Again, the lack of metallic behavior is due to excess oxygen in the film. Subsequent sputtered samples suggest that there was also excess oxygen in the sputtering chamber for Sample 1 as well.

It should be noted that no x-ray diffraction was performed on Sample 2. This is due to the conclusions drawn from the EDS and the spectroscopic ellipsometry. Because the presence of

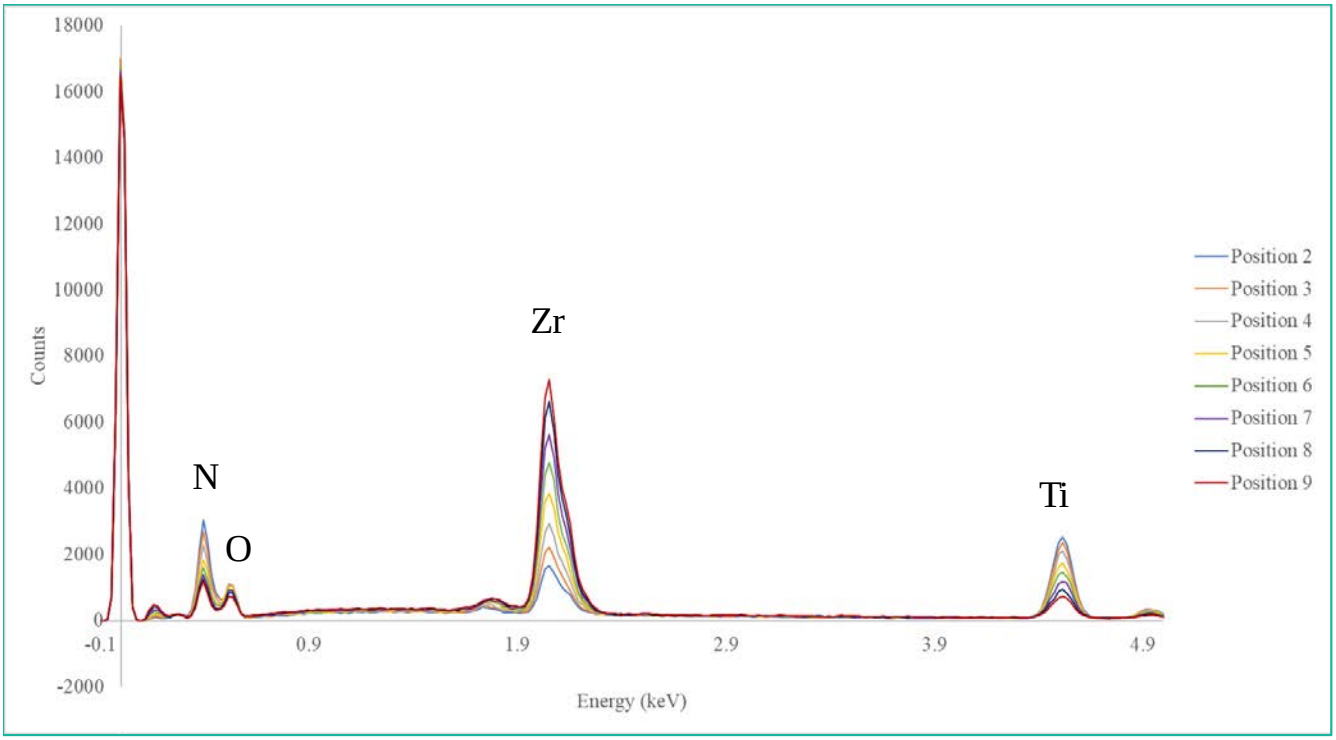

Figure 23: The EDS results for the second sputtered $Ti_xZr_{1-x}N$ sample using the ZEISS MERLIN. The peaks for N, O, Zr, and Ti were located closer to their corresponding literature values. There is no presence of a Si peak, concluding that the silicon dioxide layer was not observed during EDS analysis.

Table III: Summary of the Atomic Percent of positions 2-9 for each element. The data obtained was taken on the ZEISS MERLIN SEM instrument.

	Atomic %							
Element	**Position 2**	**Position 3**	**Position 4**	**Position 5**	**Position 6**	**Position 7**	**Position 8**	**Position 9**
Nitrogen	25.88	28.16	29.16	30.92	32.02	32.88	35.87	36.33
Oxygen	27.01	25.64	24.23	22.91	20.94	19.33	17.45	15.35
Titanium	44.5	41.52	38.89	33.95	31.08	26.08	19.65	15.97
Zirconium	2.61	4.67	7.71	12.22	15.97	21.7	27.02	32.36

oxygen in the sample had been confirmed with ellipsometry, and because it was determined that the sample did not behave metallically, no XRD was performed.

C. Sample 3

The EDS results were taken by the ZEISS MERLIN to obtain optimal peak positions. The combinatorial gradient was again observed for the third sample that was sputtered. The EDS results are displayed in Figure 26.

According to Table IV, there was a large amount of oxygen present in the film even though the combinatorial gradient had been achieved. The presence of silicon in addition to the oxygen could have caused the large spike of oxygen in the scan, due to the silicon dioxide layer on the wafer. There may have also been a leak in the oxygen line leading into the sputtering chamber. Although there is a high oxygen content, a combinatorial gradient was observed and is shown in Figure 27. The Zr content decreases as the positions increase from 1 to 9, while the Ti content increases as the positions increase. The amount of oxygen in the sputtered films follows a similar trend to the amount of Ti. This relationship is most likely due to the higher reactivity of Ti than Zr to oxygen.

Additionally, Ti is an oxyphilic metal and preferentially bonds with oxygen over nitrogen. The presence of residual

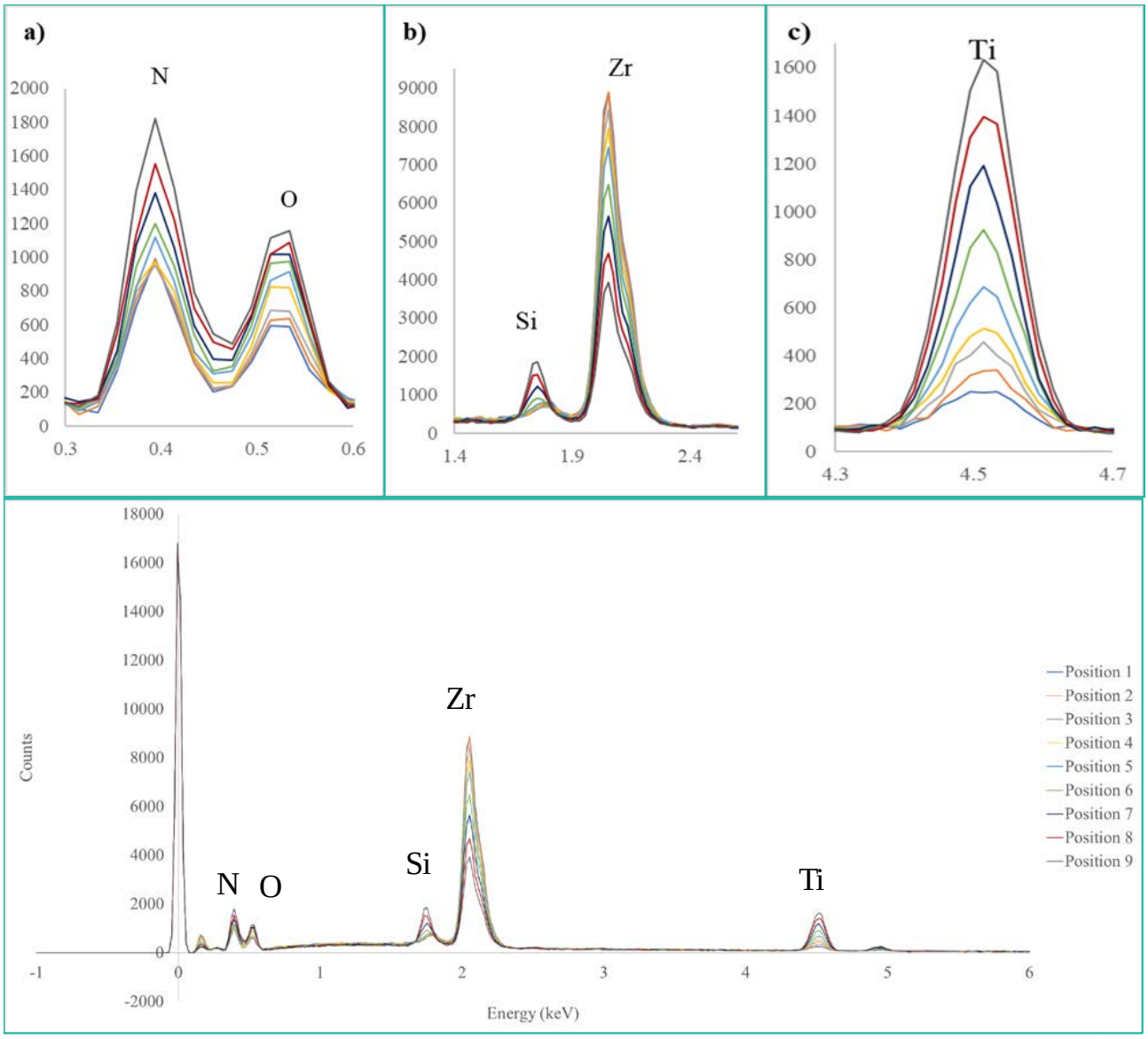

Figure 26: The EDS results for the third sputtered $Ti_xZr_{1-x}N$ sample using the ZEISS MERLIN. All the peaks are similar to the literature values. The three insets a) nitrogen (N) and oxygen (O) peaks; b) the zirconium (Zr) and silicon (Si) peaks; and c) the titanium (Ti) peaks are required for a clearer picture of the different peaks for each position. The insets show that as the positions increase from 1 to 9 the amount of Zr reduces while the amount of Ti increases.

oxygen in the chamber likely influenced how much Ti was available to bond with the nitrogen. If there was greater than 20 nTorr of residual oxygen present, the films will not behave metallically [17]. As can be seen in Figs. 21, 22, 24, 25, 29, and 30, the films did not behave metallically, indicating the presence of residual oxygen in the chamber and suggesting that the Ti preferentially bonded with oxygen instead of nitrogen. This preferential bonding explains the trend in Fig. 27.

Figure 28 shows the XRD patterns for each composition along the third as-deposited sample. A large Si peak is still present due to the substrate. Similar to the first sample, the (111) and (200) peaks shift left as the amount of Zr increases, as can be seen in Figures 28. Adding Zr to TiN increases the lattice parameter of the structure, hence the shift toward smaller 2θ positions.

The peak shift is consistent with the composition shift; however, the experimental peak positions are located outside the range of accepted literature values. This has resulted in the inability to complete Vegard's law calculations for Sample 3.

The EDS and XRD results indicated that there was no nitrogen left in the sample. Instead, a gradient formed from

Table IV: Summary of the Atomic Percent of positions 1-9 for each element for Sample 3. The data obtained was taken on the ZEISS MERLIN SEM instrument.

	Atomic %								
Elements	**Position 1**	**Position 2**	**Position 3**	**Position 4**	**Position 5**	**Position 6**	**Position 7**	**Position 8**	**Position 9**
Ti	3.8	5.76	8.22	9.75	13.55	18.77	22.96	28.33	29.26
Zr	41.49	39.67	38.11	34	30.98	26.25	20.87	16.2	11.64
N	37.15	36.9	36.07	34.32	32.95	32.45	31.88	28.98	30.36
O	11.47	12.44	14.03	16.47	18.15	20.38	21	22.09	23.25
Si	0.39	0	0.57	0.98	0.8	1.48	2.87	4.4	5.5

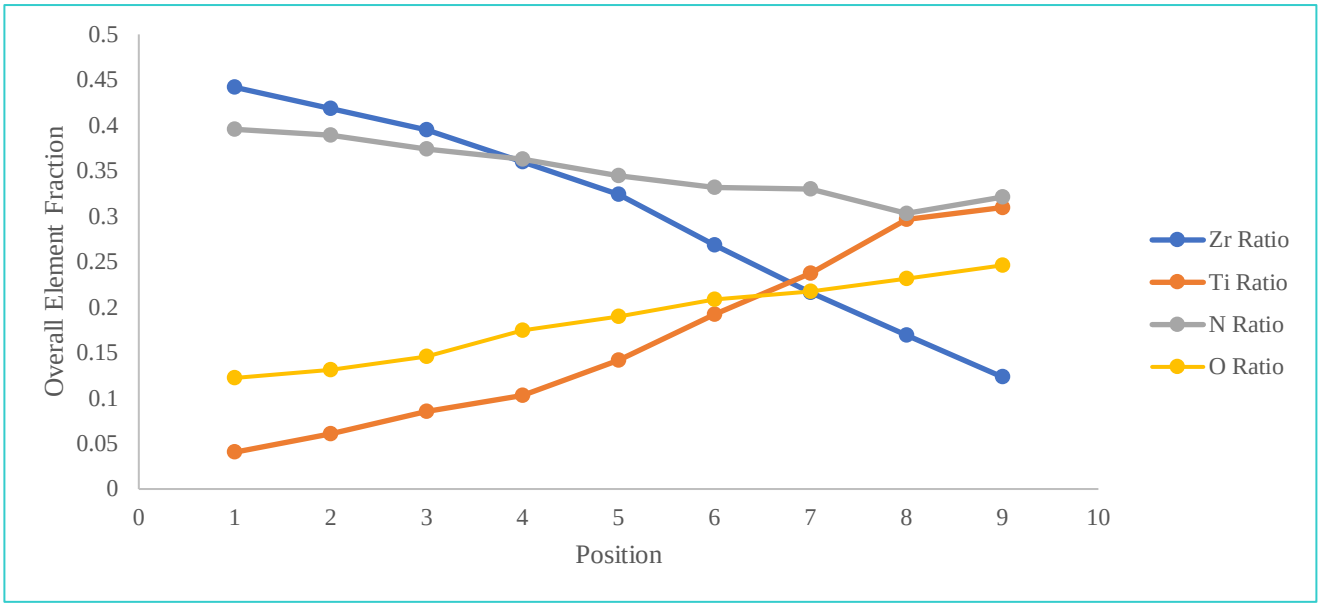

Figure 27: The overall view of the cation fractions for Ti and Zr, as well as the nitrogen fraction obtained for each position according to Table IV. The amount of nitrogen is consistent, and the combinatorial gradient is achieved.

TiO_2 to ZrO_2. Apparently, the film fully oxidized during the anneal.

In conclusion for the XRD results, a solid solution was formed over the compositional gradient in the films as observed from the consistent shifts in the (200) reflections in Figures 18, 19, and 28 as well as the (111) reflection in Figure 28. Only in the Sample 1 – 1100 °C anneal was a solid solution not identified. There is a slight peak split at position 1 for Sample 1 – 700 °C anneal that isn't seen in the as-deposited plot. This may suggest that there are two super-saturated solutions and that a secondary phase is precipitating out due to the annealing effects in the Zr-rich region. While it might be expected that there be distinct phases of TiN and ZrN present across the film, a solid solution easily forms in this ternary compound. Both TiN and ZrN resemble the rock salt crystal structure and have similar lattice constants. These compounds are highly soluble in each other and as a result, Ti and Zr are both easily exchanged in the unit cell with shifts in composition.

If two separate phases (TiN and ZrN) were present, both with the rock salt structure, then two separate sets of diffraction peaks would have been observed. The diffraction peaks would have been similar in nature but different in details including the peak positions, due to the different lattice parameter for the compounds, and intensity, due to the different number of electrons associate with Ti and Zr. Only one set of diffraction peaks were observed indicating the solid solution $Ti_{1-x}Zr_xN$ was formed.

Previous literature values obtained from several sources were averaged to compare with our results. We were able to reach the stoichiometric composition for $TiZrN_2$ (1:1 c/a ratio) at positions 5 and 6 for the as-deposited Sample 3. The 2θ positions for the (111) (36.5 2θ) [18,19] and (200) (41.2 2θ) [18,19] reflections are consistent with our results. Relative

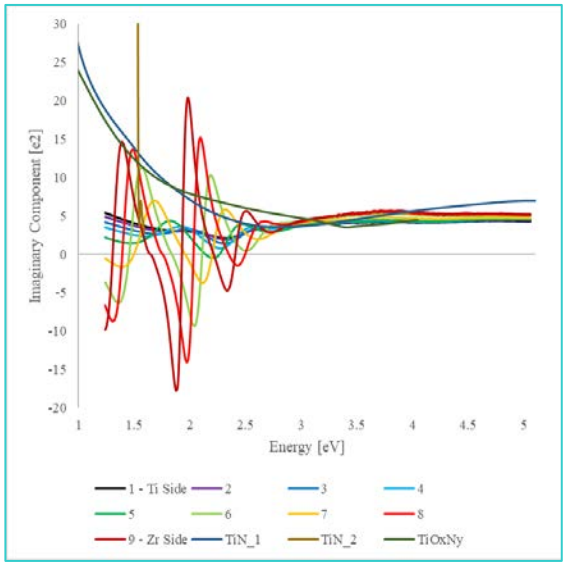

Figure 22: The imaginary component data of ellipsometry scans performed on as-deposited Sample 1.

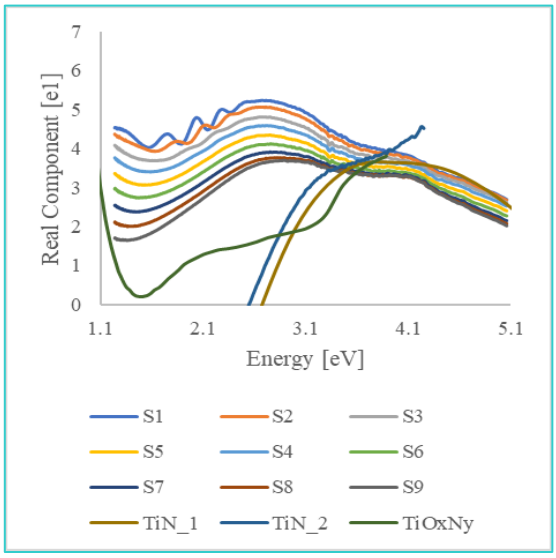

Figure 24: The real component data of ellipsometry scans performed on as-deposited Sample 2.

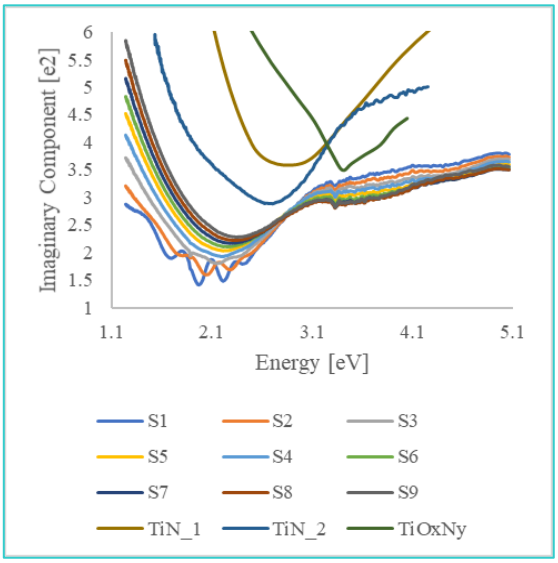

Figure 25: The imaginary component data of ellipsometry scans performed on as-deposited Sample 2.

compositions of Ti and Zr from the EDS data also correlate with a rightwards shift from positions 1-9 in the data. This is expected because as we approach the Ti-rich region of the film, the lattice parameter of TiN (4.239 Å) [20,21,22,23,24] would correspond with higher 2θ values in comparison to ZrN (4.578 Å) [25,26,27,28,29]. In the middle positions, where the stochiometric composition is approached, the literature values suggested a lattice parameter value of 4.439 Å [18,19,30,31].

An attempt to refine the lattice parameters at each position in our data using the GSAS software [32] was found to be difficult, particularly in the desired (111) reflection. This subsequently made it challenging to obtain Vegard's Law calculations. The refined lattice parameters, particularly in the middle positions, must be between that of both TiN and ZrN, but this was not the case with several attempted refinements. The refined values from the software may have indicated that variables such as sample surface displacement, transparency, and sample volume in the beam in addition to strain in the sample played roles in the discrepancy from previous literature values and peak decomposition in the (111) reflection for figures 18 and 19.

Spectroscopic ellipsometry was performed on Sample 3 as-deposited. Measurements were taken at an angle of 70°. As with Samples 1 and 2, Sample 3 is optically too thin. Visible interference patterns are still present, indicating there was still oxygen present in the sputtering chamber. The e1 values, seen in Figures 29 and 30, are still positive, indicating that this sample also does not behave metallically. Once again, the lack of metallic behavior is due to excess oxygen in the film. Optical properties were not discernable for the annealed Sample 3, as the sample had cracked and was porous after annealing.

VI. Conclusions

The EDS results for the three samples reported high levels of oxygen, most likely from oxygen contamination in the sputtering chamber. The first sample gave evidence of a thin layer of $Ti_xZr_{(1-x)}N$, although the sample was too thin for further measurements. Sample 2 did have a thicker film than Sample 1, although there were large amounts of oxygen present in the film. The combinatorial gradient was achieved for the second sample, but due to the oxygen content a third sample was sputtered. The third sample was thick enough to characterize, but again, there was a large amount of oxygen in the film. The combinatorial gradient was, however, achieved in Sample 3.

The XRD results indicate that there was a compositional gradient created during the sputtering process for Samples 1 and 3, producing a peak shift that lowered the values of 2θ as Zr replaced Ti in the lattice. Additionally, for Samples 1 and 3, the experimental peak positions were located outside of the range of accepted literature values, and Vegard's Law calculations could not be performed.

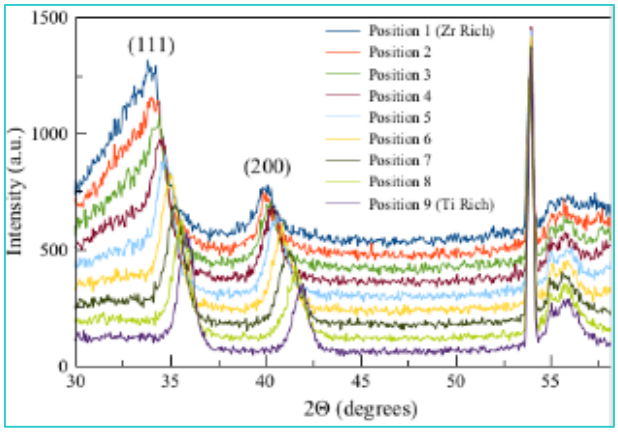

Figure 28: The diffraction pattern for the third as-deposited sample. The first prominent peak at every composition corresponds to the (111) plane, while the second, less pronounced peak corresponds to the (200) plane. The largest peak corresponds to Si.

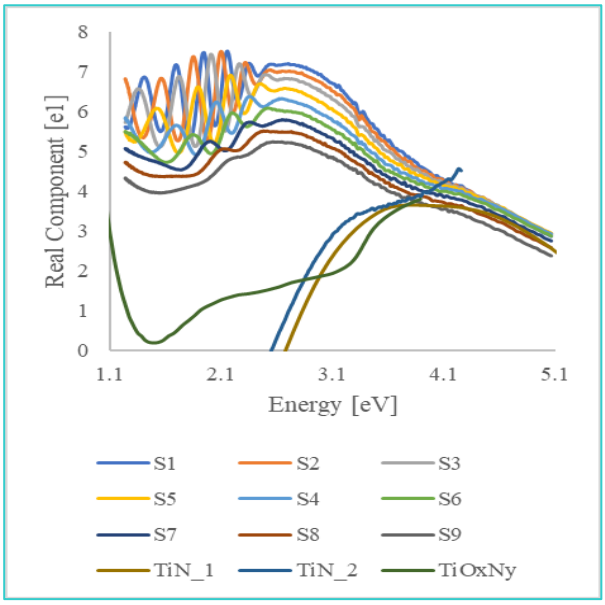

Figure 29: The real component data of ellipsometry scans performed on the as-deposited Sample 3.

The spectroscopic ellipsometry results indicate that none of the films behaved metallically. This behavior can be explained by the presence of residual oxygen in the sputtering chamber, which infiltrated the film and produced nonmetallic behavior. Additionally, Sample 3 cracked and became porous after annealing, which did not allow for optical data to be collected.

VII. Future Work

In the future, the sputtering parameters may need to be adjusted for a couple of reasons. First, none of the three films were thick enough to collect reliable ellipsometry data, resulting in interference from the silicon substrate wafers. Increasing the thickness of the film may produce better EDS and XRD results and allow for accurate characterization of the optical performance of the film. The presence of residual oxygen in the chamber also caused the Ti in the film to preferentially bond with oxygen, rather than nitrogen as expected. More closely monitoring the oxygen levels in the sputtering chamber and striving to maintain levels below 5 nTorr may produce films that behave as expected optically [17]. Finally, sputtering at higher temperatures may reduce the need to anneal the films and may lead to a solid solution and a true gradient across the film.

Acknowledgements

The group would like to thank our advisors, Dr. Philip Rack and Dr. Jason Fowlkes, for their assistance with this project. We would also like to thank David Garfinkle, Robyn Collette, Michael Koehler, Zane Palmer, and Dr. Claudia Rawn for their assistance with sample production and characterization.

References

[1] Patsalas, P., Kalfagiannis, N., Kassavetis, S., Abadias, G., Bellas, D. V., Lekka, C., & Lidorikis, E. (2017). Conductive nitrides: Growth principles, optical and electronic properties, and their perspectives in photonics and plasmonics. *Materials Science and Engineering R*, 1-55.

[2] Stockman, M. I., Kneipp, K., Bozhevolnyi, S. I., Saha, S., & Dutta, A. (2018). Roadmap on plasmonics. *Journal of Optics*.

[3] Martinez, J. G. (2018, September 14). *Plasmonic Materials: Light-controlled nanomaterials are revolutionizing sensor technology*. Retrieved from Scientific American:

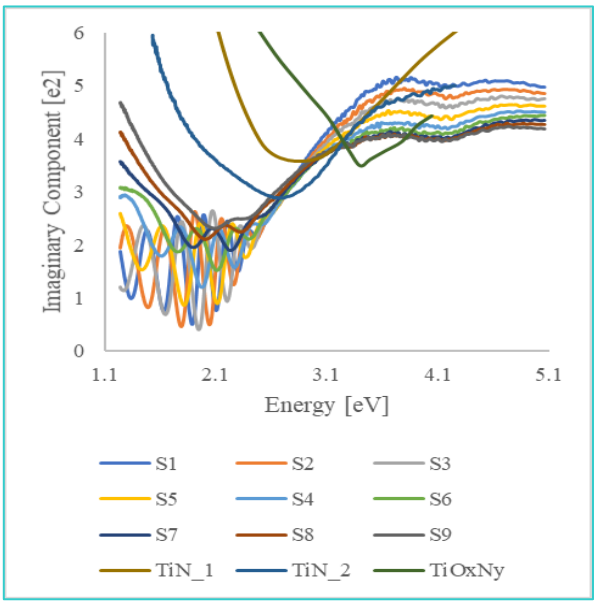

Figure 30: The imaginary component data of ellipsometry scans performed on the as-deposited Sample 3.

https://www.scientificamerican.com/article/plasmonic-materials/
[4] *Gold Nanoparticle Properties*. (2019). Retrieved from Cytodiagnostics: http://www.cytodiagnostics.com/store/pc/Gold-Nanoparticle-Properties-d2.htm
[5] *What is Sputtering?* (n.d.). Retrieved from AJA International Inc: http://www.ajaint.com/what-is-sputtering.html
[6] *What is Reactive Sputtering?* (2019). Retrieved from Semicore: http://www.semicore.com/news/67-reactive-sputtering-basics
[7] *Sputter Deposition*. (2018, May 29). Retrieved from University of Michigan LNF Wiki: http://lnf-wiki.eecs.umich.edu/wiki/Sputter_deposition
[8] Goodge, J. (2017, April 26). *Energy-Dispersive X-Ray Spectroscopy (EDS)*. Retrieved from Geochemical Instrumentation and Analysis: https://serc.carleton.edu/research_education/geochemsheets/eds.html
[9] Hafner, B. (n.d.). *Energy Dispersive Spectroscopy on the SEM: A Primer*. Retrieved from Instruments: http://www.charfac.umn.edu/instruments/eds_on_sem_primer.pdf
[10] Cullity, B. D., & Stock, S. R. (2014). *Elements of X-Ray Diffraction*. Harlow, Essex: Pearson Education Limited.
[11] Konya, T. (n.d.). *X-ray diffraction techniques for thin films*. Retrieved from http://homepage.ntu.edu.tw/~kcyuan/form/For-Rigaku-Upload_thinfilm.pdf
[12] Inaba, K. (2008). X-ray thin-film measurement techniques. *The Rigaku Journal*, 10-15. Retrieved from https://www.rigaku.com/downloads/journal/RJ24-1/RJ240102.pdf
[13] *Spectroscopic Ellipsometry: Basic Concepts*. (n.d.). Retrieved from Horiba: https://www.horiba.com/en_en/spectroscopic-ellipsometry/
[14] Butt, H.-J. K. (2006). Measurement of Adsorption Isotherms. In *Physics and Chemistry of Interfaces* (pp. 206-209). Weinheim: Wiley-VCH.
[15] Vijitha, I. (2014, November 2). *Ellipsometry*. Retrieved from SlideShare: https://www.slideshare.net/foolishcrack/ellipsometry
[16] The American Ceramic Society. (2019). Retrieved from Phase Equilibria Diagrams Online: https://phaseonline.ceramics.org/ped_figure_search/start_instructions
[17] Braic, L., Vasilantonakis, N., Mihai, A., Garcia, I. J., Fearn, S., Zou, B., . . . Petrov, P. K. (2017). Titanium Oxynitride Thin Films with Tunable Double Epsilon-Near-Zero Behavior for Nanophotonic Applications. *American Chemical Society Applied Materials & Interfaces*, 29857-29862.
[18] Kieffer, R.; Nowotny, H.; Ettmayer, P.; Dufek, G., Metall (Clausthal-Zellerfeld, Germany) (1972) 26, (7) p701-p708
[19] Duwez, Pol; Odell, Francis, Journal of the Electrochemical Society (1950) 97, (10) p299-p304
[20] Bannister, F.A. Osbornite, meteoric titanium nitride. Mineralogical Magazine (1941) 26, (*) p36-p44.
[21] Hofmann, W.; Schrader, A. Titancarbid in grauem Gusseisen. Archiv fuer das Eisenhuettenwesen (1936) 10, (*) p65-p66.
[22] Schoenberg, N. An X-ray investigation on ternary phases in the Ta-Me-N systems (Me = Ti, Cr, Mn, Fe, Co, Ni). Acta Chemica Scandinavica (1954) 8, (*) p213-p220.
[23] Holleck, H.; Smailos, E. Mischnitride von Thorium mit Seltenen Erden. Journal of Nuclear Materials (1980) 91, (1) p237-p239.
[24] Jiang, Chorn-Cherng; Goto, Takashi; Hirai, Toshio. Non-stoichiometry of titanium nitride plates prepared by chemical vapour deposition. Journal of Alloys and Compounds (1993) 190, (2) p197-p200.
[25] Acta Chemica Scandinavica, Series A: Physical ad Inorganic Chemistry (1975) 29, (*) p563-p568
[26] Baker, T.W. The coefficient of thermal expansion of Zirconium nitride. Acta Crystallographica (1958) 11, (*) p300-p300
[27] Timofeeva, I.I.; Shvedova, L.K. Microhardness and thermal expansion of transition metal nitrides at 80-300 K. Izvestiya Akademii Nauk SSSR, Neorganicheskie Materialy (1972) 8, (*) p1027-p1029
[28] Yang Xiao; Takeichi, N.; Shida, K.; Tanaka, H.; Kuriyama, N.; Sakai, T. Novel Mg-Zr-A-H (A=Li, Na) hydrides synthesized by a high pressure technique and their hydrogen storage properties. Journal of Alloys and Compounds (2011) 509, (*) p1211-p1216
[29] Gusev, A.I.; Shveikin, G.P. Solid solutions in the system ZrN-NbC. Inorganic Materials (1974) 10, (7) p1087-p1089
[30] Hoerling, A., Sjolen, J., Willmann, H., Larsson, T., Oden, M., & Hultman, L. (2008). Thermal stability, microstructure and mechanical properties of Ti1-xZrxN thin films. Thin Solid Films,516(18), 6421-6431.
[31] Yu-Wei, L., Chia-Wei, L., Ge-Ping, Y., & Jia-Hong, H. (2016). Structure and Properties of Nanocrystalline (TiZr)x N1-x Thin Films Deposited by DC Unbalanced Magnetron Sputtering. Journal of Nanomaterials, 2016, Journal of Nanomaterials, 2016, Vol.2016.
[32] B.H. Toby and R.B Von Dreele, "GSAS-II: the genesis of a modern open-source all purpose crystallography software package",Journal of Applied Crystallography,46, 544-549(2013).

APPENDIX I: SAMPLE IMAGES

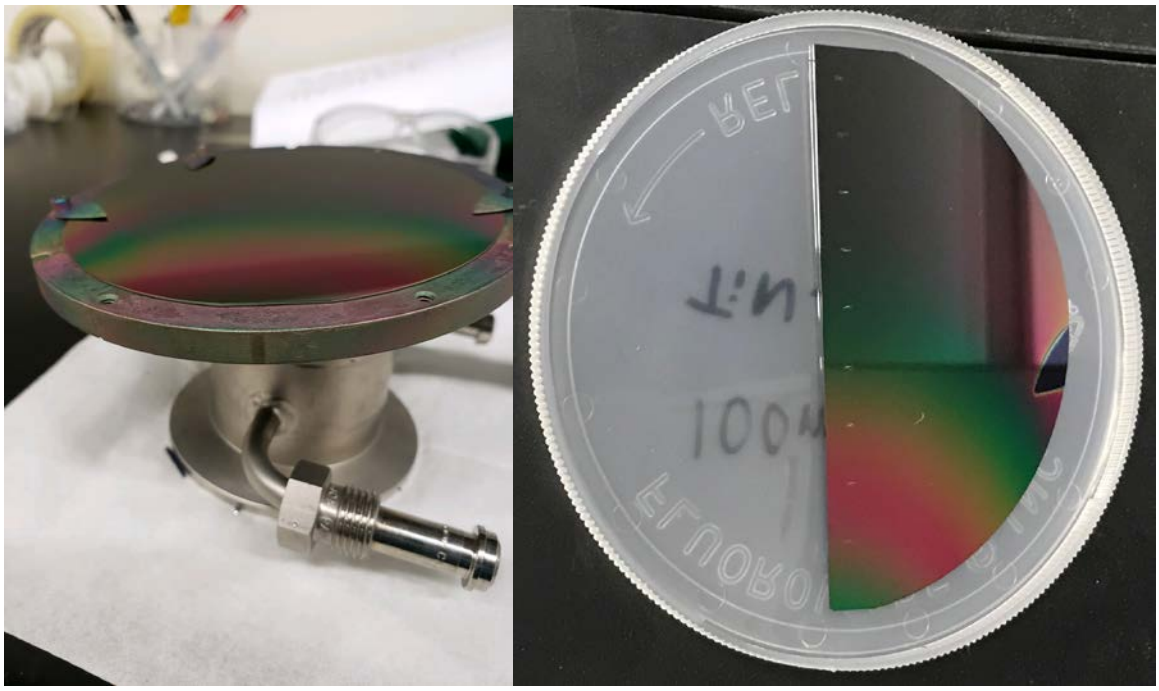

Figure 31: Sample 1; (Left) immediately after sputtering; (Right) cut in half and marked, with position 1 at the bottom of the sample and position 8 at the top of the sample.

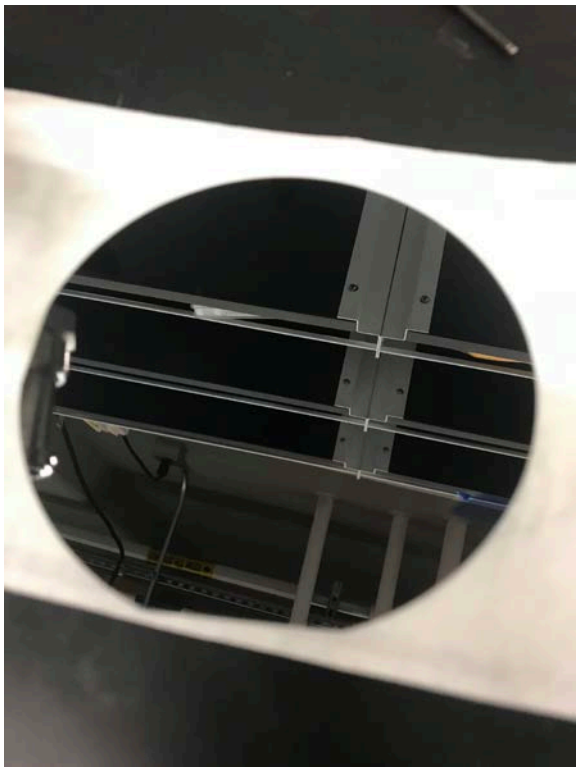

Figure 32: Sample 2; the gradient is less obvious due the amount of oxygen in the sample.

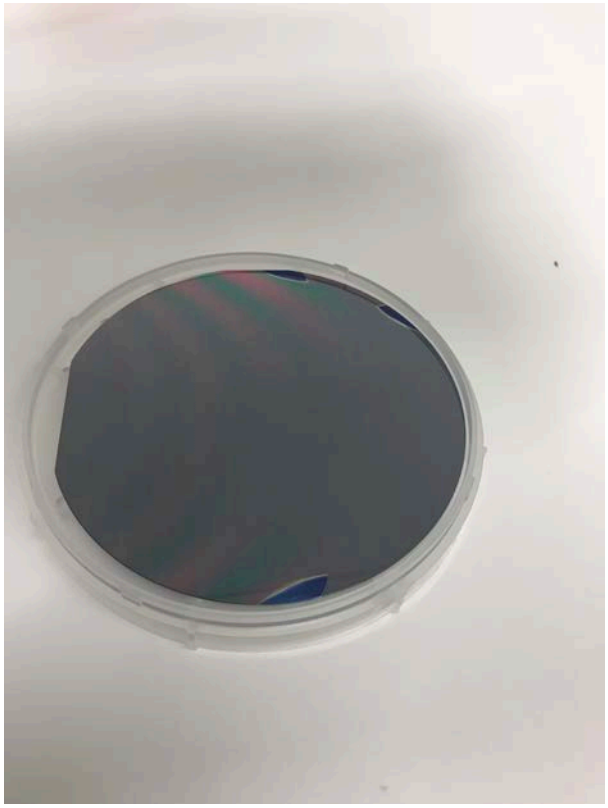

Figure 33: Sample 3; the gradient is less noticeable than Sample 1, but still clearer than Sample 2.

APPENDIX II: SPUTTERING IMAGES

Figure 34: (Left) Sputtering targets before nitrogen was flowed into the chamber; (Right) sputtering targets after Nitrogen was flowed into the chamber. It is easier to distinguish between the two metal targets in the image on the right.